MULTI-IMAGE SHAPE-FROM-SHADING: DERIVATION OF PLANETARY DIGITAL TERRAIN MODELS USING CLEMENTINE IMAGES

Volker Lohse, Christian Heipke

University of Hannover, Institute of Photogrammetry and GeoInformation, Nienburger Straße 1, 30167 Hannover, Germany - (lohse, heipke)@ipi.uni-hannover.de

Commission IV, WG 9

KEY WORDS: High-resolution DTM, extraterrestrial surfaces, reconstruction method.

ABSTRACT:

In many cases, the derivation of high-resolution digital terrain models (DTMs) from planetary surfaces using only conventional digital image matching is a problem. The matching methods need at least a stereo pair of images covering an area with sufficient texture. Often though, space missions provide only a few stereo images and planetary surfaces often possess insufficient texture.
This paper describes a method for the generation of high-resolution DTMs from planetary surfaces using digital optical images developed by the authors over a number of years. The suggested method, termed "multi-image shape-from-shading" (MI-SFS), is able to generate a planetary DTM with an arbitrary number of images of low texture. Therefore, MI-SFS is a suitable method in areas, in which image matching fails to yield a DTM.
The paper contains a short review of the theory of MI-SFS, followed by a presentation of results, which were obtained with images from NASA's lunar mission Clementine. These results constitute the first practical application of MI-SFS using extraterrestrial imagery. The reconstruction of the lunar surface is made with the assumption of different kinds of reflectance models (Lommel-Seeliger and Lambert model). The represented work shows that the derivation of a high-resolution DTM of real digital planetary images by means of MI-SFS is feasible.

1. INTRODUCTION

Digital terrain models (DTMs) are an important information source for many applications in planetary sciences, such as for the description of local and regional topographic features, slopes, discontinuities of the surface and thus possible flow direction of liquid material and isostatic considerations to name only a few. On Earth, such DTMs can normally be generated by means of conventional photogrammetry including digital image matching. But planetary missions in general are not topographic missions, and therefore usually only a few stereoscopic images are available. Additionally, some planetary stereo pairs have a disadvantageous camera configuration (e.g. a poor base-to-height ratio or different images resolutions) and in many cases planetary images have poor image texture, which is an obstacle to automatic matching methods. For this reason, in many regions no complete high-resolution DTM of planetary bodies can be made available by means of conventional photogrammetric methods.

Besides photogrammetry, there are other methods to generate a DTM of a planetary body. One example is laser scanning as employed by the "Mars Orbiter Laser Altimeter" (MOLA) flown on the Mars Global Surveyor mission (Smith et al., 2001). MOLA acquired high-precision height information along one dimensional tracks, but despite simultaneous processing of multiple orbits, the horizontal resolution of the resulting data set is rather limited.

For these reasons, it is of great interest to many planetary scientists to have at their disposal reconstruction methods, which are able to work with a single image and/or with images including low texture, such as "multi-image shape-from-shading" (MI-SFS).

MI-SFS has been developed by our group over the last years. A detailed description including results with simulated and aerial images from a desert area on Earth are given in (Heipke, 1992; Heipke, Piechullek, 1994; Piechullek, 2000). First investigations with real digital planetary images from NASA's lunar mission Clementine of 1994 are presented in (Lohse, Heipke, 2003). This paper deals with advanced results using Clementine images. Similar investigations, however with the goal to produce orthophoto mosaics from images taken at different illumination directions, are described in (Dorrer, 2002). Other approaches worth mentioning are the iterative multi-image DTM reconstruction by (Gaskell, 2003) and the integration of image matching and shape-from-shading suggested by (Fua, Leclerc., 1995).

2. MULTI-IMAGE SHAPE-FROM-SHADING

For solving the DTM reconstruction problem by SFS, the image formation process has to be modelled and inverted with respect to the parameters describing the object space (Horn et al., 1989). Like other SFS methods, MI-SFS is based on the fact that surface patches, having different inclination relative to the light source, are imaged with different brightness. MI-SFS uses these variations in the grey values for the reconstruction of the surface. In contrast to classical SFS methods, MI-SFS can deal with an arbitrary number of images and spectral bands, is based on a perspective transformation between image and object space and relates directly the grey values to the heights of a DTM and the parameters of a radiometric model, which describes the surface reflectance behaviour. The DTM heights as well as the parameters of the radiometric model are estimated from the image grey values in a least-squares adjustment.

For MI-SFS it is assumed that the albedo in the observed area is constant everywhere, because the method does not differ

between albedo and topographical variations as reason for grey value changes in image space.

For the mathematical modelling of the bi-directional reflectance (BDR), we use the Lunar-Lambert model (McEwen, 1991) for describing the object surface. This radiometric model is a linear combination of two different models, the Lambert and the Lommel-Seeliger model.

The Lambert law is one of the simplest and most frequently used reflectance models. Specific descriptions and equations of the Lambert law can be found in (Horn, 1986; Hapke, 1993; Zhang et al., 1999). The Lambert law describes a surface, which emits the incoming irradiance uniformly in all directions. The model is based on the assumption that the brightness of a surface depends only on the incidence angle i, the angle between the direction of illumination $\vec{s}$ and the surface normal $\vec{n}$ (figure 1). This means, that a surface looks equally bright from every viewing direction. The Lambert model characterizes the reflectance from bright surfaces very well.

The second used radiometric model is the Lommel-Seeliger law. In order to extend the assumption that light reflection occurs at the boundary surface between two media only, the Lommel-Seeliger law was derived by Seeliger (Horn et al., 1989; Hapke, 1993; Rebhan, 1993). In this model, light scattering is assumed to take place at the individual particles within a layer of infinite thickness below the apparent surface; the irradiance observed at a sensor comes from light scattered by all particles in the medium lying within the field of view of the sensor. Therefore, the Lommel-Seeliger law does not only contain i but also the emittance angle e between viewing direction $\vec{v}$ and $\vec{n}$ (figure 1). The significant increase in brightness for large e is due to the fact that with increasing e the area of the imaged surface also increases, and consequently a greater part of the surface layer contributes to the brightness observed in the sensor. In contrast to the Lambert law, the Lommel-Seeliger law describes dark surfaces better.

Using first only the Lommel-Seeliger reflectance the model grey value $G(x',y')$ in image space can be formulated based on the well-known camera equation (e.g. Horn, 1986):

$$G(x',y') = k\frac{\pi}{4}\cos^{a}(\gamma)\left(\frac{d}{f}\right)^{2} E_s\rho(X,Y)\frac{2\cos(i)}{\cos(i)+\cos(e)} \qquad (1)$$

with $$\cos(e) = \frac{\vec{n}\,\vec{v}}{|\vec{n}|\,|\vec{v}|} \quad \text{and} \quad \cos(i) = \frac{\vec{n}\,\vec{s}}{|\vec{n}|\,|\vec{s}|}$$

where

$G(x',y')$	model grey value at image point P'
x',y'	image coordinates of P' (proj. of P into image space)
k	rescaling constant for transformation of image irradiance into model grey value G(x',y')
a	exponent of light fall-off
γ	angle between optical axis and the ray through P and P'
d	aperture of optical lens
f	focal length of optical lens
E_S	scene irradiance
$\rho(X,Y)$	albedo of the object surface at P(X,Y,Z)
$\vec{n}$	normal vector of the object surface at P(X,Y,Z)
$\vec{s}$	vector in illumination direction at P(X,Y,Z)
$\vec{v}$	vector in viewing direction at P(X,Y,Z)

The scene irradiance E_S, the parameters (a, d, f, k and γ) and the albedo ρ are assumed to be constant values and are merged into a so called reflectance coefficient A_R:

$$A_R = k\frac{\pi}{4}\cos^{a}(\gamma)\left(\frac{d}{f}\right)^{2} E_s\rho(X,Y) \qquad (2)$$

Thus, the model grey value G depends on A_R, $\vec{s}$, $\vec{v}$ and $\vec{n}$:

$$G(x',y') = f(A_R,\vec{s},\vec{v},\vec{n}) = A_R\frac{2\cos(i)}{\cos(i)+\cos(e)} \qquad (3)$$

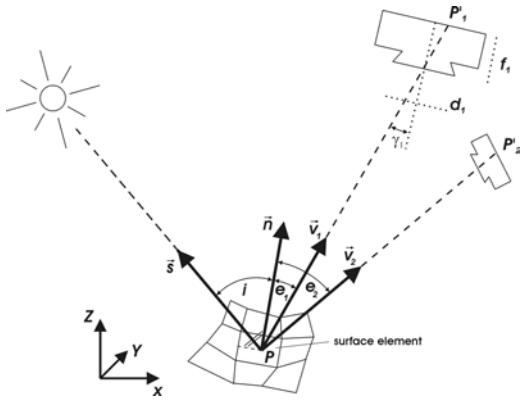

Figure 1. Configuration of multiple images, camera parameters and the relationship between $\vec{s}$, $\vec{n}$, $\vec{v}$

In the case of the Lunar-Lambert model the model grey value G looks as follows:

$$G(x',y') = A_R\left[2\Lambda\frac{\cos(i)}{\cos(i)+\cos(e)}+(1-\Lambda)\cos(i)\right] \qquad (4)$$

The parameter Λ controls the weighting between the Lambert and the Lommel-Seeliger term. The light source in this approach is assumed to be a distant point with a known position. The influences of a possibly existing atmosphere are considered to be constant, and thus part of A_R. Moreover, the parameters of the interior and the exterior orientation are assumed to be known from a camera calibration and a previously carried out bundle adjustment.

For the purpose of the object surface description, a geometrical and a radiometrical surface model are introduced. The mathematical description of the geometric model is given by means of a DTM with a simple grid structure, which is defined in the XY-plane of the object space. The roughness of the terrain is the decisive point for the choice of the mesh size of the grid. An independent height $Z(X_k,Y_l)$ is assigned to each grid point (X_k,Y_l) of the DTM. A height Z at an arbitrary point is interpolated from the neighbouring grid heights, e.g. by bilinear interpolation. At each point of the object surface, $\vec{n}$ and thus the angles i and e become a function of the neighbouring $Z_{k,l}$.

A radiometric surface model is introduced to establish the connection between the geometric surface model and the reflectance behaviour of the surface. Each DTM grid mesh is divided into several object surface elements of constant size. The size is chosen approximately equal to the pixel size multiplied by the average image scale factor. Each object surface element is assigned the same reflectance coefficient A_R.

Since we assume, that $\vec{s}$ and the parameters of orientation of all images j, and thus also all $\vec{v}_j$, are known, the only unknown parameters for the computation of $G(x',y')$ (equation 4) are the parameters of the object surface model, the DTM heights $Z_{k,l}$ and A_R. Each considered object surface element can be projected into the image space of each used image j using the well known collinearity equations. At the resulting position $P_j'(x',y')$ the image grey value $g_j(x',y')$ can be resampled from the recorded grey values. The g_j are considered as observations in a least-squares adjustment for the estimation of the unknowns. The corresponding observation equations read:

$$v_j(x',y') = G\left(\hat{Z}_{k,l}, \hat{A}_R\right) - g_j\left(x'\left(\hat{Z}_{k,l}\right), y'\left(\hat{Z}_{k,l}\right)\right) \quad (5)$$

where $v_j(x',y')$ residuals of observed grey value in image j

$\hat{Z}_{k,l}$ DTM-heights (k – column; l – row), unknown

$\hat{A}_R$ reflectance coefficient, unknown

G model grey value

g_j observed grey value in image j

After inserting equation (4) into equation (5) we obtain:

$$v_j(x',y') = \hat{A}_R\left[\Lambda\frac{2\cos\left(i_j\left(\hat{Z}_{k,l}\right)\right)}{\cos\left(i_j\left(\hat{Z}_{k,l}\right)\right)+\cos\left(e_j\left(\hat{Z}_{k,l}\right)\right)} + (1-\Lambda)\cos\left(i_j\left(\hat{Z}_{k,l}\right)\right)\right] - g_j\left(x'\left(\hat{Z}_{k,l}\right), y'\left(\hat{Z}_{k,l}\right)\right) \quad (6)$$

Equation (6) is non-linear with regard to $\hat{Z}_{k,l}$, and for this reason initial values have to be available for the unknown object space parameters $\hat{Z}_{k,l}$ and $\hat{A}_R$ for carrying out the least-squares adjustment.

3. MI-SFS INVESTIGATIONS

In order to investigate the proposed method with real extraterrestrial imagery we have selected suitable overlapping images from NASA's 1994 scientific lunar mission Clementine. A detailed description of the Clementine mission is published in (Nozette et al., 1994).

At the beginning of this section we investigate and discuss the case of a one-image analysis by means of MI-SFS. After that, we carry out the multiple-image analysis and determine the radius of convergence of the method.

3.1 Input data

For the reconstruction of a surface by means of MI-SFS it is necessary that following information and data is available:

- one or more digital images
- interior and exterior orientation of the images
- sun position during data acquisition for each image
- initial values for the unknowns (heights $Z_{k,l}$ and A_R)

For our investigations we selected images from the Ultraviolet/Visible (UV/Vis) digital frame camera, a medium resolution camera based on CCD-technology. We chose two images (figure 2) which were taken from different orbits. Image no. 334 is an oblique image with an off nadir angle of approximately 12.2 degrees. The second image no. 338 was recorded when the camera was tilted sidewards over the same region with an off nadir angle of about 46.8 degrees. The two images were recorded with a time difference of 20 hours. We assume that during this period of time no changes happened in the observed area. The mean geometric resolution of a pixel in both images is about 180 m. In the overlapping part of the two images an area with a size of 24.3 x 24.3 km^2 was chosen. The altitude difference in this region is about 1.3 km. The selected area of the moon is part of the "Northern Mare Orientale Basin" (between 16.3° and 14.3° South and 87.3° and 90.9° West) and is depicted as the white rectangles in the two images (figure 2). The area is divided into 54 x 54 DTM grids with a mesh size of 450 m. Thus, in total there are 3025 DTM-heights. Each grid mesh consisted of 3 x 3 object surface elements with a size of 150 x 150 m^2.

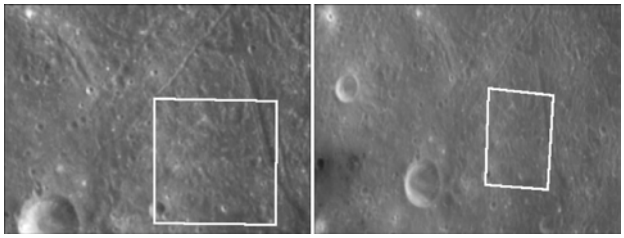

Figure 2. Selected images: no. 334 (l.), no. 338 (r.)

3.2 One-image analysis

In the following, we carried out analyses with one image; assuming Lambert (L) and Lommel-Seeliger reflectance (LS). This means, that Λ, the weighting parameter for the ratio of the two models, takes the value zero and the value one, respectively.

We introduce a manually measured DTM as initial-DTM. This DTM was measured several times by different operators using a digital photogrammetric workstation. For the unknown reflectance coefficient A_R we use the mean grey value of the input images as initial value.

The internal accuracy of the manually measured DTM is about 80 metres. However, the stereo configuration of the images was not optimal and for this reason the measurement of the DTM cannot be regarded as reference. Nevertheless, we compared the obtained DTMs with the manually measured DTM to calculate the mean offset Z_0 and the standard deviation *rms* (table 1). These parameters include the inaccuracy of the initial-DTM. For the interpretation of the accuracy parameters it should be noted that the mean position change in the two images of about one pixel (pixel size of 23 µm) conforms with a height change in the DTM of approximately 360 metres.

No.	Image	Model	Absolute DTM-height	Iterations	Z_0 [m]	rms [m]
1	338	L	corner	no conv.	-	-
2	334	L	corner	no conv.	-	-
3	338	LS	corner	13	14.7	156.1
4	334	LS	corner	no conv.	-	-
5	338	LS	centre	16	19.3	156.9
6	338	LS	edge	14	8.9	158.3

Table 1. Results of the one-image analyses

With the assumption of a Lambert surface the calculations diverge. Analysis no. 3 assuming a Lommel-Seeliger surface converges after 13 iterations. The *rms* value lies below a half

pixel in image space and is in the range of the measurement accuracy of the initial DTM. With this knowledge we conclude that the observed area seems to be a Lommel-Seeliger rather than a Lambert surface. The analysis with image 334, assuming Lommel-Seeliger, does not converge. Reasons for this behaviour are discussed in section 3.3.

From one image the scale factor between image and object coordinate system cannot be determined. Therefore, we fix one DTM-height at the boundary of the observed area as constant, to guarantee the determination of absolute DTM-heights. The reason for choosing a boundary position is, that if there is height information for the regarded surface, then these height values come in all probability from the neighbouring region with sufficient texture computed by means of image matching. To demonstrate that the algorithm is independent of the chosen position of the introduced absolute DTM-height, we carried out analysis no. 3 (table 1) with two other heights. Analysis no. 5 is computed with a constant height at the centre and analysis no. 6 with a height at the middle of an edge. The normally used constant DTM-height lies at a corner of the observed area.

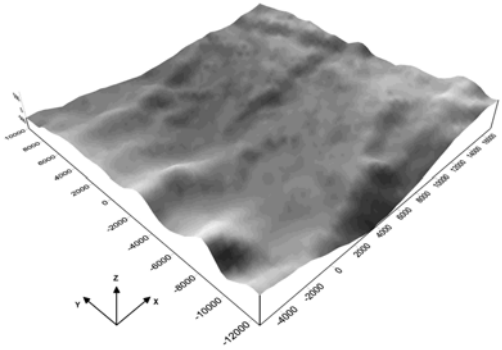

Figure 3. Resulting $DTM_{LS,\ 338}$ (height-exaggeration factor 2x)

Figure 3 shows $DTM_{LS,\ 338}$ of analysis no. 3. A comparison of the orthoimage and the model grey values, both computed with the initial DTM, and the model grey values, computed with $DTM_{LS,\ 338}$, is shown in figure 4.

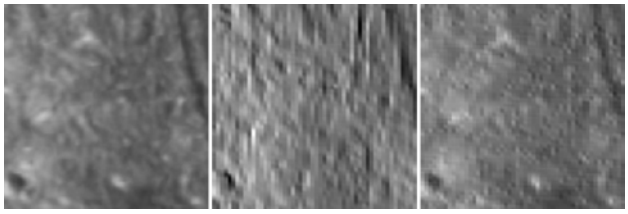

Figure 4. Image 338: orthoimage (l.), model grey values of initial DTM (m.) and of $DTM_{LS,\ 338}$ (r.)

In the model grey values of the initial DTM, vertical striping effects along the measuring directions of the operator can be seen. This demonstrates that the manually measured DTM is not of high accuracy. The resulting $DTM_{LS,\ 338}$ corresponds much better to the orthoimage (figure 4 left and right), although a few visible structures in the images, such as craters and valleys, are not visible in $DTM_{LS,\ 338}$. In a comparison of an enlargement of the model grey values of $DTM_{LS,\ 338}$ and the same enlarged area of the orthoimage (figure 5 centre and right) some blobs and grid structures are visible. The grid structures are an indication, that the chosen meshes of the geometric surface model may not be sufficiently small. We are still investigating possible reasons for the visible blobs.

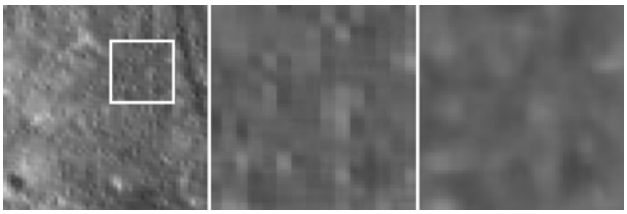

Figure 5. Model grey values of $DTM_{LS,\ 338}$ (l.), enlargement of marked area (m.) and same area in orthoimage (r.)

3.3 Error diagnostics

In this section we go into the matter of the non-convergence using image 334 assuming Lommel-Seeliger reflectance. A comparison of the orthoimage and the model grey values calculated with the initial DTM (figure 6) shows, that the grey value differences are extremely large. The model grey values are 22 percent darker than the observed grey values. This is probably a reason that the algorithm computes wrong DTM-heights and diverges.

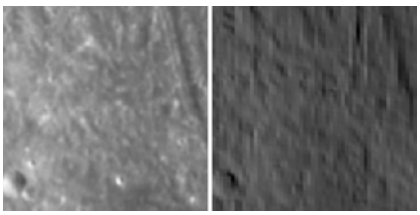

Figure 6. Image 334: orthoimage (l.), model grey values (r.)

The following causes are possible reasons for the large grey value differences:

- incorrect radiometric calibration of image no. 334
- assumption of a wrong reflectance model

With the given information there is no way to separate these effects from each other. The only possibility is to adjust the observed values to the model using a simple mathematical transformation without investigating the physical meaning. To compensate the encountered radiometric problems a change of the grey values in image 334 as described in table 2, is carried out.

Mean model grey value G $[W \cdot sr^{-1} \cdot m^{-2}]$		Mean grey value of orthoimage g $[W \cdot sr^{-1} \cdot m^{-2}]$
3.28		4.20
$G = a_0 + m \cdot g$		
Modification	Offset a_0 $[W \cdot sr^{-1} \cdot m^{-2}]$	Scale factor m
m1	0.00	0.78
m2	2.06	0.29

Table 2. Modification parameters for image 334

The first modification method m1 is a change of the grey values in image 334 with only a scale factor. The second variant m2 is a linear accommodation of the grey values. The simplest concept, only an offset, is not useful, because due to the fact the G is a linear function of A_R (see equation 4) after using the first iteration the correction of the unknown reflectance coefficient is the same as the offset computed a priori. Table 3 shows the results computed with the modified image 334.

The computation diverges if we use only the scale factor. If we use the linear change, the algorithm converges. In comparison to the analysis with image 338 the result with image 334m2 is

not very good. Also the high number of required iterations is an indication of a relatively poor result. Compared to the analysis with image 334, however, this result is a significant improvement. It should be recalled that the obtained *rms* corresponds to only $^2/_3$ of a pixel. Figure 7 shows the orthoimage and the model grey values, both computed with the initial DTM, and the model grey values, computed with $DTM_{LS,\ 334m2}$.

Image	Comment	Iterations	Z_0 [m]	rms [m]
334m1	only scale factor	no conv.	no conv.	no conv.
334m2	linearly changed	42	79.5	242.7

Table 3. Results with modified image 334

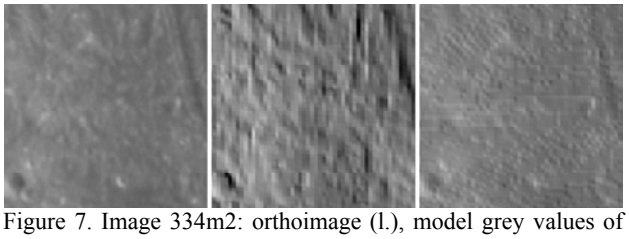

Figure 7. Image 334m2: orthoimage (l.), model grey values of initial DTM (m.) and of $DTM_{LS,\ 334m2}$ (r.)

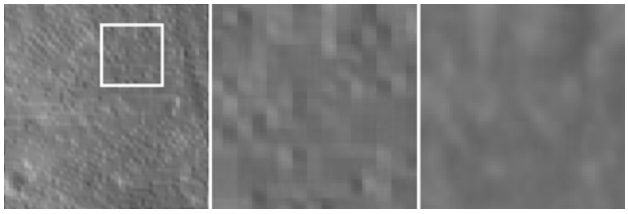

Figure 8. Model grey values of $DTM_{LS,\ 334m2}$ (l.), enlargement of marked area (m.) and same area in orthoimage (r.)

The orthoimage shows less contrast than the orthoimage in figure 6. This happens, due to the used scale factor ($m \approx 0.3$). At the beginning the model grey values show the already reported strips caused by manual measurement (figure 7 centre). The model grey values computed with $DTM_{LS,\ 334m2}$ (figure 7 right and figure 8 centre) show again some blobs. The resulting $DTM_{LS,\ 334m2}$ is illustrated in figure 9.

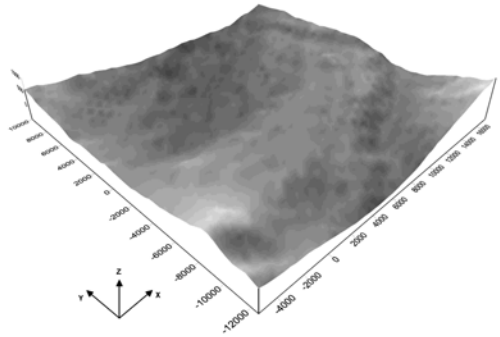

Figure 9. $DTM_{LS,\ 334m2}$ (height-exaggeration factor 2x)

In comparison with $DTM_{LS,\ 338}$ (figure 3), $DTM_{LS,\ 334m2}$ exposes the consequences of contrast reduction of image 334. The resulting DTM is smoothed.

In order to demonstrate that the linear modification applied to image no. 334 does not have a negative effect if orthoimage and model grey values are of approximately equal brightness, we have also applied the modification to image no. 338. As expected, the result does not show significant changes to the computation with the original image (see analysis no. 3, table 1). After 19 iterations the accuracy parameter Z_0 has the value of 42.6 metres and a *rms* of about 148.7 metres.

3.4 Two-image analysis

The advantage of applications using multiple images with different exterior orientations is that an additional geometric stabilisation constraint, the correspondence between the images, is added to the determination of the surface. In addition, further images provide independent grey value information for the reconstruction of the unknown DTM heights. Compared with the one-image analysis, it is unnecessary to introduce a known height as a scale factor, because homologous image rays intersect in the appropriate object point. In this way, the definition of absolute heights is guaranteed.

If we use the two described original images, the computation failed as expected. For this reason, we carried out the two-image analysis using the modified images 334m2 and 338m3. The analysis converges after only four iterations (table 4).

Images	Comment	Iterations	Z_0 [m]	rms [m]
334m2 / 338m3	linearly changed	4	-19.2	140.1

Table 4. Result of a two-image analysis using modified images

The fast computation and the values of the accuracy parameters are indications of a good reconstruction. $DTM_{LS,\ 334m2,\ 338m3}$ (figure 10) shows that the poor grey value information of image 334 could be overcome by the second image.

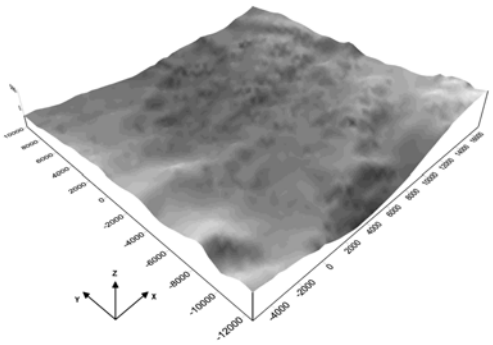

Figure 10. $DTM_{LS,\ 334m2,\ 338m3}$ (height-exaggeration factor 2x)

3.5 Radius of convergence

To investigate the radius of convergence of MI-SFS, we have inserted different initial DTMs into the algorithm. These DTMs differ from the manually measured DTM by an offset a_0 and a scale factor m. The height differences are chosen in a way that the mean position change of a surface element in the two images is a multiple of the pixel size. As mentioned in section 3.2, a pixel change in the images conforms with a height change of about 360 metres. Using equation 7, 15 different initial DTMs were computed (table 5).

The results of the two-image analyses assuming Lommel-Seeliger reflectance and computed with different initial DTMs are presented in table 5. The numerical results show, that the radius of convergence of MI-SFS is approximately four pixels which conforms with an offset a_0 of about 1440 metres. It should be noted, that the algorithm produces a correct result also starting from a horizontal plane located at the average height in the investigated area (third line of table 5).

$$Z_{Xi} = \bar{Z}_M + a_0 + m\left(Z_{Mi} - \bar{Z}_M\right) \quad (7)$$

where $\bar{Z}_M$ mean value of the manually measured DTM
Z_{Mi} DTM-height no. i of the manually measured DTM
Z_{Xi} DTM-height no. i of the destination DTM_X
m scale factor
a_0 height offset

DTM parameter		Analysis and accuracy parameter		
Scale factor m	Offset a_0 [m]	Iterations	Z_0 [m]	rms [m]
1	0.0	4	-19.2	140.1
0.5	0.0	9	-8.4	146.3
0	0.0	7	-9.5	150.5
1	360.0	6	36,3	148.4
0.5	360.0	18	14.2	145.4
1	720.0	12	35.4	148.4
0.5	720.0	14	15.6	143.1
1	1080.0	18	16.5	142.3
0.5	1080.0	16	21.4	143.6
1	1440.0	29	11.6	141.7
0.5	1440.0	26	16.5	142.6
1	1800.0	17	1801.9	1807.9
0.5	1800.0	83	14.5	147.0
1	2160.0	10	2184.9	2190.2
0.5	2160.0	18	2174.5	2181.4

Table 5. Radius of convergence using two images

4. CONCLUSIONS

The represented work on MI-SFS shows that the derivation of a high-resolution DTM of real digital planetary images by means of MI-SFS is feasible. The one-image and multiple-image analyses are carried out using imagery from the lunar mission Clementine. The obtained results shows that MI-SFS is a method which is able to close the gaps in DTMs determined with other reconstruction methods. Furthermore we show, that the required initial values have a radius of convergence of about four pixels (in this case of about 1440 metres).

The computation with one of the images was not successful. In this case we developed a simple, and successful method which modified the observed grey values. In order to do so, we also needed an initial-DTM of the area, and although we have not yet explicitly checked this assumption, we believe that we can compute the grey value modification based on the DTM which serves as initial height values for the whole approach.

In future we will intensify our investigations to simultaneously process two and more images within MI-SFS. We will also try to increase the geometric accuracy by introducing more sophisticated object surface models (one times one pixel DTMs with appropriate smoothness constraints, breakline and occlusion detection modules). We also plan to integrate the line sensor geometry into the algorithm, to use other planetary data, e.g. HRSC data. In addition, the next important step is the combination of image matching with MI-SFS into a combined method. A precondition for such a combination is a separation of the surface under consideration into parts with constant albedo (MI-SFS) and into parts with variable albedo (image matching). This task remains a challenge of the whole approach which we will try to tackle using texture analysis.

5. REFERENCES

Dorrer, E., 2002. Digital Elevation Model Refinement by Shape-from-Shading. *Bildteknik/Image Science*, Stockholm, Nr. 2002:1, pp. 57-67.

Fua, P., Leclerc, Y. G., 1995. Object-Centered Surface Reconstruction: Combining Multi-Image Stereo and Shading. *International Journal of Computer Vision*, 16, pp.35-56.

Gaskell, R. W., 2003. Optical only determination of small body shape and topography. *ISPRS Extraterrestrial Mapping Workshop "Advances in Planetary Mapping 2003"*, Houston.

Hapke, B., 1993. Theory of Reflectance and Emittance Spectroscopy, Topics in remote sensing Vol. 3, New York, Cambridge University Press.

Heipke, C., 1992. Integration of digital image matching and multi image shape from shading. *ISPRS*, Washington, Vol. XXIX, Part B3, pp. 832-841.

Heipke, C., Piechullek, C., 1994. Towards surface reconstruction using multi image shape from shading. *ISPRS*, Vol. XXX, Part 3/1, pp. 361-369.

Horn, B. K. P., 1986. *Robot Vision*. The MIT Press, 509 p.

Horn, B. K. P., Brooks, M. J., 1989. *Shape from Shading*, The MIT Press, 577 p.

Lohse, V., Heipke, C., 2003. Derivation of digital terrain models by means of multi-image shape-from-shading: results with Clementine images. *ISPRS Workshop "High Resolution Mapping from Space 2003*", CD-ROM, University of Hannover.

McEwen, A. S., 1991. Photometric Functions for Photoclinometry and Other Applications. *Icarus 92*, pp. 298-311.

Nozette, P. et al., 1994. The Clementine mission of the moon. *Science*, Vol. 266, pp. 1835-1839.

Piechullek, C., 2000. Oberflächenrekonstruktion mit Hilfe von einer Mehrbild-Shape-from-Shading-Methode. *Deutsche Geodätische Kommission*, Reihe C, Heft 518, 96 p.

Rebhan, H., 1993. Richtungsabhängige Reflexions-eigenschaften der lunaren Oberfläche. *Dissertation*, München, DLR-Forschungsbericht 93-28.

Smith, D. E., et al., 2001. Mars Orbiter Laser Altimeter: Experiment summary after the first year of global mapping of Mars. *Journal of Geophys. Res.*, 106 (E10), pp. 23689-23722

Zhang, R. et al., 1999. Shape from Shading: A Survey. *IEEE Trans, PA&MI*, Vol. 21, pp. 670-706.

6. ACKNOWLEDGEMENT

This work was developed within the priority program "Mars and the terrestrial planets" financed by the Deutsche Forschungsgemeinschaft (DFG) under the project number HE 1822/10. The support is gratefully acknowledged. Thanks also go to DLR for providing the Clementine data, and to the employees of the ISIS Support Center at the United States Geological Survey (USGS) for their aid in the radiometric calibration of the Clementine images.